J. Fluid Mech. (2003), *vol.* 497, *pp.* 289–317.
DOI: 10.1017/S0022112003006670 Printed in the United Kingdom

The onset of three-dimensional standing and modulated travelling waves in a periodically driven cavity flow

By H. M. BLACKBURN[1] AND J. M. LOPEZ[2]

[1]CSIRO Manufacturing and Infrastructure Technology, PO Box 56, Highett, Vic 3190, Australia

[2]Department of Mathematics and Statistics, Arizona State University, Tempe, AZ 85287, USA

(Received 22 November 2002 and in revised form 19 August 2003)

Three-dimensional instabilities of the two-dimensional flow in a rectangular cavity driven by the simple harmonic oscillation of one wall are investigated. The cavity has an aspect ratio of 2:1 in cross-section and is infinite in the spanwise direction. The two-dimensional base flow has no component in the spanwise direction and is periodic in time. In addition, it has the same space–time symmetry as a two-dimensional periodically shedding bluff-body wake: invariance to a mid-plane reflection composed with a half-period evolution in time. As for the wake, there are two kinds of possible synchronous three-dimensional instability; one kind preserves this space–time symmetry and the other breaks it, replacing it with another space–time symmetry. One of these symmetry breaking modes has been observed experimentally. The present study is numerical, using both linear Floquet analysis techniques and fully nonlinear computations. A new synchronous mode is found, in addition to the experimentally observed mode. These two modes have very different spanwise wavelengths. In analogy to the three-dimensional instabilities of bluff-body wakes, the long-wavelength synchronous instability is named mode A, while that for the short wavelength is named mode B. However, their space–time symmetries are interchanged compared to those of the synchronous bluff-body wake modes. Another new, but non-synchronous, mode is found: this has complex-conjugate pair Floquet multipliers, and arises through a Neimark–Sacker bifurcation of the base flow. This mode, QP, has a spanwise wavelength intermediate between modes A and B, and manifests itself in the nonlinear regime as either quasi-periodic standing waves or modulated travelling waves.

1. Introduction

In their experimental study, Vogel, Hirsa & Lopez (2003) describe the vortex dynamics of the flow in a rectangular cavity that is driven by the harmonic oscillation of the bottom wall. The original motivation for studying that flow stems from its potential use in measurement of surface dilatational viscosity of a gas/liquid interface in the presence of insoluble monolayers (Lopez & Hirsa 2001). For that application, the top lid is removed to expose a free interface. For practical operation of the surface viscometer, it is desirable to have the flow in its basic state (i.e. nominally two-dimensional with a flat interface). Vogel *et al.* experimentally examined the stability of the basic state, both with a free surface and with a rigid top lid. The spanwise extent of the cavity was large, approximately 20 times the depth of the cavity. As might be expected for flows in large-aspect-ratio geometries, it was observed that the effects of the spanwise sidewalls were small and localized, at least for the basic state. The expectation

was further confirmed by comparing the experimentally observed flows at low forcing amplitude with two-dimensional computations. The primary features of the two-dimensional time-periodic basic state consist of a Stokes layer on the oscillating wall that is forced to roll-up into vortical rollers by the presence of the streamwise endwalls; the rollers form alternately at each end of the cavity, synchronously with the stroke of the bottom. The experiments showed that, in the range of parameters considered, the two-dimensional basic state lost stability to a three-dimensional state with a well-defined periodicity in the spanwise direction. This spanwise periodicity was observed to vary smoothly with parameter changes, suggesting that quantization effects due to the finite spanwise length were not significant.

Those observations helped to motivate the present study into the stability of the two-dimensional basic state to three-dimensional disturbances, periodic in the spanwise direction, for a cavity with a rigid top lid. As work progressed, it became apparent that further interest is engendered through the connection to the stability properties of other flows that share the same symmetry group, e.g. two-dimensional time-periodic wakes of bluff bodies such as the circular and square cylinders. While those flows are autonomous and open, whereas this flow is periodically driven and completely enclosed, the connections between the primary symmetry breaking transitions in both classes of flow appear to be quite direct. The distinction between open and closed flow is not important because the wake instabilities are of absolute type. The fact that the present flow is periodically driven, while the two-dimensional wakes are autonomous, does, however, have an important consequence. In the wake flows, there is only one dimensionless controlling parameter, the Reynolds number, whereas in the cavity flow (with a fixed geometry) there are two, since both the amplitude and frequency of the wall motion can be varied independently. As a result, we can independently produce onset of all the modes we have observed through appropriate choices for these control parameters. This is different to what occurs in the wake flows: for example, in the circular cylinder wake, 'mode A' is the first three-dimensional instability to arise as Re is increased ($Re \approx 190$) and 'mode B' bifurcates at higher Re from a basic state that is already unstable to mode A.

Through Floquet analysis of the cavity flow we have found that the basic state loses stability to three-dimensional modes in a number of distinct ways, depending on the parameter regime. Specifically, we have identified two synchronous modes that are analogous to modes A and B of circular and square cylinder wakes (Williamson 1988, 1996; Barkley & Henderson 1996; Robichaux, Balachandar & Vanka 1999), together with a new quasi-periodic three-dimensional mode which can manifest either as standing waves, or spanwise travelling waves that are modulated by the periodic base flow.† Of these two, only the travelling-wave solutions are stable.

1.1. *Flow geometry, dimensionless groups, and symmetries*

Figure 1 is a schematic of the cavity showing the Cartesian coordinate system (x, y, z) and instantaneous isosurfaces of the spanwise z-vorticity of a two-dimensional basic state at the end of the stroke of the oscillating cavity floor in the y-direction. The naming and orientation of the axes have been chosen in order to help underscore the connection of the symmetries of the present flow with those of bluff-body wakes, in which the free-stream flow is conventionally aligned in the x-direction. The two-dimensional system has two characteristic lengths: the cavity x-dimension h and its

† In another study (Blackburn & Lopez 2003), we have shown that the two-dimensional wakes of the circular and square cylinder both possess standing-wave and travelling-wave modes.

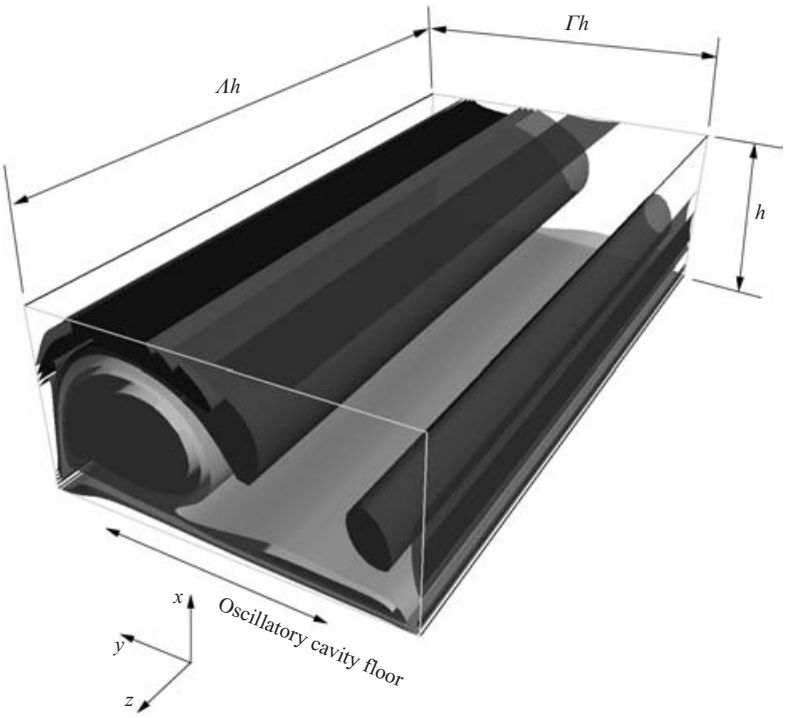

FIGURE 1. Schematic of the cavity showing the coordinate system and instantaneous isosurfaces of the spanwise z-vorticity of a basic state.

y-dimension Γh. Taking h as a length scale, the maximum floor velocity V_{max} as a velocity scale, the period T of sinusoidal floor oscillation as a time scale, and the fluid's kinematic viscosity, ν, we have three dimensionless groups that completely govern the flow. These are the cavity aspect ratio Γ, the Reynolds number

$$Re = V_{max}\, h/\nu,$$

and the Stokes number

$$St = h^2/T\nu.$$

We keep the streamwise aspect ratio fixed at $\Gamma = 2$ as this is the value used in the experiments of Vogel *et al.* (2003), which in addition had spanwise aspect ratio $\Lambda = 19$. The y-velocity of the wall at $x = 0$ is given by $V_{max} \sin(2\pi t/T)$.

The basic flow state will have the symmetries of the system. For finite Λ, the geometry is a rectangular box, but such a system does not have the symmetry of a rectangular box, owing to the periodic oscillation of the floor. The only spatial invariance of this flow in a finite rectangular box is reflection about $z = 0$:

$$(u, v, w)(x, y, z, t) = (u, v, -w)(x, y, -z, t), \tag{1.1}$$

i.e. Z_2 symmetry. In the limit $\Lambda \to \infty$, the spatial invariances are reflections about any (x, y)-plane and arbitrary translations in the spanwise z-direction,

$$(u, v, w)(x, y, z, t) = (u, v, w)(x, y, z + \alpha, t), \tag{1.2}$$

for any real α, which in combination with (1.1), and assuming spanwise periodicity, generates an $O(2)$ spanwise symmetry group. The harmonic oscillation of the floor

in the cavity introduces a spatio-temporal symmetry. The system is invariant to a reflection about the plane $y=0$ together with a half-period evolution in time:

$$(u, v, w)(x, y, z, t) = (u, -v, w)(x, -y, z, t + T/2), \tag{1.3}$$

where $T = (Re\, h)/(St\, V_{max})$ is the period of the floor oscillation. This spatio-temporal symmetry – which we shall refer to as H symmetry – is isomorphic to Z_2. So the complete symmetry group of the flows we have studied here is $O(2) \times Z_2$. The individual symmetries, and their group, are exactly the same as for two-dimensional time-periodic wakes of symmetrical bluff bodies such as the circular and square cylinders.

1.2. *Implications of symmetries for instabilities*

The time-periodic base flow may lose stability in a number of ways. One is via a synchronous bifurcation, whereby a Floquet multiplier crosses the unit circle at $+1$, and a new time-periodic state synchronous with the floor oscillation results. The breaking of reflection symmetry in the spanwise direction corresponds to a pitchfork bifurcation, but the associated translation invariance in the $O(2)$ symmetry means that we have a pitchfork of revolution, the individual solutions being distinguished by their spatial phase in the spanwise direction. The solutions would correspond to a family of standing waves (modulated by the base flow in our case), with periodic structure in the spanwise direction. Modes A and B of the circular cylinder wake are of this type.

Another possibility is for a pair of complex-conjugate multipliers to cross the unit circle, giving rise to a quasi-periodic state, one period being that of the floor oscillation and the other related to the phase angle of the pair of critical Floquet multipliers that attain unit modulus at the Neimark–Sacker bifurcation. For our problem, the new second frequency can manifest itself in two ways, depending on whether the bifurcation breaks the spanwise reflection invariance or the spanwise translation invariance of the $O(2)$ symmetry of the basic state. If spanwise reflection invariance is broken, then the bifurcating state is a $+z$- or $-z$-travelling wave (TW), modulated by the oscillating base state. The spanwise translation speed is proportional to the new frequency resulting from the bifurcation. The two possibilities ($\pm z$-TW) are related by the spanwise reflection symmetry. If instead, the bifurcation breaks the spanwise translation invariance, then quasi-periodic standing waves (SW) result. In this case, a complete circle of standing waves results, distinguished by their spanwise spatial phase. As in the case of a Hopf bifurcation with $O(2)$ symmetry (Golubitsky, Stewart & Schaeffer 1988), the Neimark–Sacker bifurcation with $O(2)$ symmetry results in both SW and TW bifurcating simultaneously.

The third way that this system may lose stability is via a period doubling bifurcation, whereby pairs of critical Floquet multipliers cross the unit circle at -1; the work of Swift & Wiesenfeld (1984) shows that in systems with H-symmetry, two is the minimum multiplicity required. As a consequence of the additional $O(2)$ spanwise symmetry in our problem, the minimum required multiplicity of the -1 multiplier for period doubling is four, and further, the period doubling is a codimension-two bifurcation (Marques, Lopez & Blackburn 2003). Such a bifurcation has, to our knowledge, not yet been recorded for flows with $Z_2 \times O(2)$ symmetry.

A more extended explanation of the implications of the present base flow symmetry group for the possible kinds of three-dimensional symmetry-breaking bifurcations may be found in Marques *et al.* (2003).

2. Floquet analysis and modal structure

The Floquet stability analysis on which this work is based in turn rests on time evolution of the incompressible Navier–Stokes equations and their linearized equivalents for the evolution of infinitesimal perturbations about the T-periodic two-dimensional base flows. The interested reader can find background and more detail in Iooss & Joseph (1990), Barkley & Henderson (1996) and Tuckerman & Barkley (2000). The main focus of this section will be the Fourier spanwise structure and symmetries of Floquet modes.

Perturbation solutions $\boldsymbol{u}'$ can be written as a sum of Floquet modes, $\breve{\boldsymbol{u}}(t+t_0) = \mathrm{e}^{\gamma t}\tilde{\boldsymbol{u}}(t_0)$, where $\tilde{\boldsymbol{u}}(t_0)$ are the T-periodic Floquet eigenfunctions of the Navier–Stokes equations linearized about the T-periodic base flow, t_0 is an arbitrary starting phase and the constants $\gamma = \sigma + \mathrm{i}\omega$ are Floquet exponents. The Floquet multipliers, which define the growth of Floquet modes over one base flow period, are related to the exponents by $\mu = \mathrm{e}^{\gamma T}$. The time-periodic basic state becomes linearly unstable when one or more multipliers leaves the unit circle, or equivalently when the real part of one or more exponents becomes positive. In a Neimark–Sacker bifurcation, the imaginary part, ω, of the Floquet exponent is non-zero, signalling the introduction of a second period $T_s = 2\pi/\omega$ into the mode – in general, T_s is incommensurate with T and the mode is quasi-periodic. It is convenient in the development below to define also the normalized Floquet mode, in which the exponential growth is factored out, leaving a possibly oscillatory temporal behaviour:

$$\bar{\boldsymbol{u}}(t+t_0) = \mathrm{e}^{-\sigma t}\breve{\boldsymbol{u}}(t+t_0) = \mathrm{e}^{\mathrm{i}\omega t}\tilde{\boldsymbol{u}}(t_0). \tag{2.1}$$

The base flow $\boldsymbol{U}$ here is both two-dimensional, i.e. $\partial_z \boldsymbol{U} = 0$, and two-component, i.e. $\boldsymbol{U} \equiv (U, V, 0)$. These restrictions have important implications for the three-dimensional spatial forms that the Floquet modes can take. The three-dimensional structure of the eigenfunctions is expressed by their projection onto a Fourier basis in z: at each wavenumber $\beta = 2\pi h/\lambda$, where λ is the wavelength in the z-direction,

$$\tilde{\boldsymbol{u}}(x, y, z, t) = \hat{\boldsymbol{u}}(x, y, t)\mathrm{e}^{\mathrm{i}\beta z} + \hat{\boldsymbol{u}}^{\star}(x, y, t)\mathrm{e}^{-\mathrm{i}\beta z}, \tag{2.2}$$

where $\hat{\boldsymbol{u}}^{\star}$ is the complex-conjugate of $\hat{\boldsymbol{u}}$. With a two-dimensional two-component restriction of the base flow $\boldsymbol{U}$, restricted three-dimensional mode shapes of the two forms

$$(u', v', w')(x, y, z, t) = (u'\cos\beta z, v'\cos\beta z, w'\sin\beta z)(x, y, t), \tag{2.3}$$

$$(u', v', w')(x, y, z, t) = (u'\sin\beta z, v'\sin\beta z, w'\cos\beta z)(x, y, t), \tag{2.4}$$

are linearly independent. For cases with real Floquet multipliers, it is sufficient to examine the behaviour of either of these forms, since any linear combination will just correspond to moving the reference frame a fixed distance in the spanwise direction. However, for quasi-periodic modes – those for which the Floquet exponents/multipliers have a non-zero imaginary part – restricting the mode shapes to one of (2.3) or (2.4) corresponds to a restriction to standing-wave type solutions. Consider the temporal evolution of a normalized Floquet mode for a quasi-periodic case (complex-conjugate Floquet multipliers), where now scalar $\bar{u}$ represents any of $(\bar{u}, \bar{v}, \bar{w})(x, y, z, t)$ and dropping reference to the arbitrary starting phase t_0,

$$\begin{aligned}\bar{u}(x, y, z, t) &= [\hat{u}(x, y)\mathrm{e}^{\mathrm{i}\beta z} + \hat{u}^{\star}(x, y)\mathrm{e}^{-\mathrm{i}\beta z}]\mathrm{e}^{\mathrm{i}\omega t} + [\hat{u}(x, y)\mathrm{e}^{\mathrm{i}\beta z} + \hat{u}^{\star}(x, y)\mathrm{e}^{-\mathrm{i}\beta z}]\mathrm{e}^{-\mathrm{i}\omega t} \\ &= [\mathrm{e}^{\mathrm{i}\omega t} + \mathrm{e}^{-\mathrm{i}\omega t}]\mathrm{e}^{i\beta z}\hat{u}(x, y) + [\mathrm{e}^{\mathrm{i}\omega t} + \mathrm{e}^{-\mathrm{i}\omega t}]\mathrm{e}^{-i\beta z}\hat{u}^{\star}(x, y).\end{aligned} \tag{2.5}$$

This general form allows travelling waves (TWs) to be represented. Restriction to cosine waves in z implies taking $\hat{u}^\star = \hat{u}$ real, and thus

$$\begin{aligned}\bar{u}(x, y, z, t) &= \left[\mathrm{e}^{\mathrm{i}(\omega t+\beta z)} + \mathrm{e}^{-\mathrm{i}(\omega t+\beta z)} + \mathrm{e}^{\mathrm{i}(\omega t-\beta z)} + \mathrm{e}^{-\mathrm{i}(\omega t-\beta z)}\right]\hat{u}(x, y) \\ &= 4\cos\beta z\cos\omega t\,\hat{u}(x, y),\end{aligned} \tag{2.6}$$

a standing cosinusoidal wave. Likewise, restriction to sine waves in z implies taking $\hat{u} = -\hat{u}^\star$ purely imaginary, and so

$$\begin{aligned}\bar{u}(x, y, z, t) &= \left[-\mathrm{i}\mathrm{e}^{\mathrm{i}(\omega t+\beta z)} + \mathrm{i}\mathrm{e}^{-\mathrm{i}(\omega t+\beta z)} - \mathrm{i}\mathrm{e}^{\mathrm{i}(\omega t-\beta z)} + \mathrm{i}\mathrm{e}^{-\mathrm{i}(\omega t-\beta z)}\right]\hat{u}(x, y) \\ &= 4\sin\beta z\cos\omega t\,\hat{u}(x, y),\end{aligned} \tag{2.7}$$

again, a standing wave (SW), this time with sinusoidal structure in z. So to allow travelling-wave Floquet modes for cases where critical multipliers come in complex-conjugate pairs, we have to allow a full complex structure for $\hat{\boldsymbol{u}}$. By restricting the symmetries of the modes we can also compute standing-wave cases.

3. Numerical techniques

3.1. *Treatment of the evolution equations*

All the numerical techniques rely on time evolution of the Navier–Stokes equations and their linearized equivalents, using standard spectral element methods in (x, y) and Fourier expansions in the spanwise z-direction for three-dimensional direct numerical simulation (DNS). See Karniadakis (1990), Karniadakis & Sherwin (1999) and Henderson (1999) for other examples and detailed descriptions of the associated numerical methods.

3.1.1. *Boundary conditions*

Non-slip velocity boundary conditions are employed on all walls. The velocity is zero on stationary walls, and the perturbation velocity is zero on all walls. In the two-dimensional simulations used to compute the base flows for stability analysis, and in the three-dimensional simulations of the evolved flows, the y-component of velocity, v, on the oscillating floor was set to

$$v(0, y, z, t) = [1-\exp(-200(1+y/h)^4)][1-\exp(-200(1-y/h)^4)]V_{max}\sin(2\pi t/T), \tag{3.1}$$

the exponential terms provide a smooth regularization of the discontinuity where the floor meets the stationary walls.

Pressure boundary conditions are obtained by taking the dot product of the domain unit outward normal $\boldsymbol{n}$ with the Navier–Stokes equations. For each Fourier mode k

$$\partial_n \hat{P}_k = \boldsymbol{n}\cdot(-\widehat{\boldsymbol{A}\boldsymbol{u}}_k - \nu\nabla\times\nabla\times\hat{\boldsymbol{u}}_k - \partial_t\hat{\boldsymbol{u}}_k), \tag{3.2}$$

where $\widehat{\boldsymbol{A}\boldsymbol{u}}_k$ represents the Fourier transform of the advection terms in either the full or linearized Navier–Stokes equations, the rotational form of the viscous term exploits the solenoidality of the velocity, and for the present application $\boldsymbol{n}\cdot\partial_t\boldsymbol{u} = 0$ at all boundaries.

3.1.2. *Discretization and convergence*

The spectral element mesh employed in the (x, y)-plane is illustrated in figure 2. Time integration uses a mixed explicit–implicit time-stepping scheme with equal-order velocity and pressure shape functions (Karniadakis, Israeli & Orszag 1991), and all results presented here were obtained using second-order time integration.

Within each spectral element, shape functions in (x, y) are tensor products of Gauss–Legendre–Lobatto (GLL) Lagrange nodal interpolants. The order of the

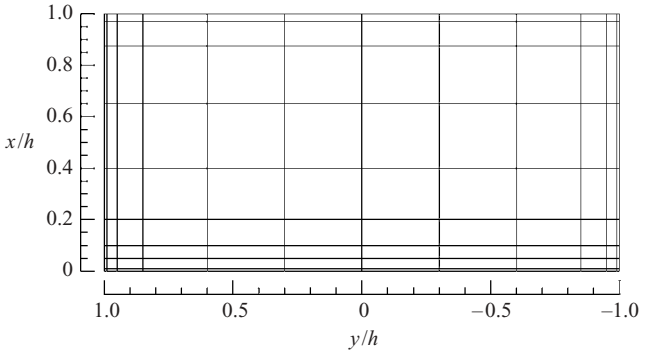

FIGURE 2. Cross-section of the cavity in the (x, y)-plane, showing the outlines of the 108 spectral elements used in the discretization. The oscillating wall is located at $x = 0$.

		(10, 738)		(100, 1212)		(200, 1250)	
N_p	N_{tot}	$1000E_{min}$	$1000E_{max}$	$1000E_{min}$	$1000E_{max}$	$1000E_{min}$	$1000E_{max}$
3	1126	6.4235	35.841	7.4178	16.716	4.9522	10.000
5	2806	6.4614	36.150	7.7386	17.013	4.2900	11.106
7	5440	6.4612	36.154	7.7354	17.010	4.2966	11.111
9	10800	6.4612	36.154	7.7337	17.009	4.2958	11.111

TABLE 1. Spatial resolution convergence study of the two-dimensional base flows, showing the effect of varying the GLL Lagrange polynomial order N_p on temporal maxima and minima of the flow kinetic energy at three representative combinations of the control variables (St, Re).

one-dimensional Lagrange interpolants, N_p, was selected on the basis of two-dimensional convergence tests for integrating the Navier–Stokes equations, conducted at a range of representative values of St and Re, with the monitored parameter being the kinetic energy of the flow, E. These results are shown in table 1. The total number of independent mesh points in two dimensions for each interpolation order is given by N_{tot}. At each combination of control parameters (which effectively bracket those used in the remainder of the paper), the maxima and minima of the kinetic energy have converged to three significant figures or better at $N_p = 7$, which was adopted for all subsequent simulations.

For three-dimensional Navier–Stokes simulations, the spanwise wavelength $\lambda = 2\pi h/\beta$ used at each studied combination of (St, Re) was chosen as the most-amplified wavelength found in related Floquet analyses. The number of modes adopted was chosen after simulations were conducted with 16 Fourier modes (spanwise mesh spacing $\lambda/32$). On the basis that the minimum decay in spectral energy at Fourier mode index $k = 3$ compared to the two-dimensional component at $k = 0$ was seven orders of magnitude, eight z-planes (four Fourier modes) was deemed sufficient for subsequent three-dimensional simulations.

3.2. *Floquet analysis*

3.2.1. *Numerical method*

Floquet analysis for three-dimensional instabilities is carried out using the linearized Poincaré map for the T-periodic two-dimensional base flows. The numerical method employed has been described by Barkley & Henderson (1996), Tuckerman & Barkley (2000); Krylov subspace iteration is used to extract the dominant eigenvalues of the

		(10, 738); $\beta = 8.25$		(100, 1212); $\beta = 9.00$		(200, 1250); $\beta = 1.75$	
N_p	N_{tot}	$\lvert\mu\rvert$	$\angle\theta$	$\lvert\mu\rvert$	$\angle\theta$	$\lvert\mu\rvert$	$\angle\theta$
3	1126	0.4234	0	0.7756	$\pm$1.4628	0.9295	0
5	2806	0.9684	0	1.0241	$\pm$1.4471	1.0014	0
7	5440	0.9859	0	0.9944	$\pm$1.4723	1.0018	0
9	10 800	0.9862	0	0.9905	$\pm$1.4771	1.0015	0

TABLE 2. Spatial resolution convergence study for Floquet analysis, showing the effect of varying the GLL Lagrange polynomial order N_p on Floquet multipliers at the same combinations of the control variables St and Re used in the two-dimensional resolution studies summarized in table 1, and at particular values of β, as shown. Complex-conjugate Floquet multipliers are indicated by non-zero values of θ in the polar form.

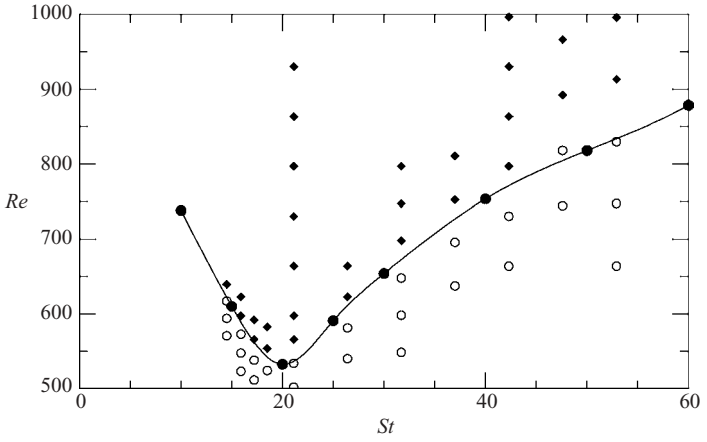

FIGURE 3. The locus in parameter space of the transition from the two-dimensional base state to the three-dimensional mode B state, as determined by Floquet analysis (solid circles and line), together with experimental observations (Vogel *et al.* 2003): open circles represent two-dimensional states, filled diamonds represent three-dimensional mode B states.

map. The data used to supply the T-periodic base flow are obtained through Fourier-series reconstruction from a limited number (typically 64) of time-slices obtained from two-dimensional DNS.

3.2.2. *Validation and resolution studies*

The spatial convergence of the Floquet analysis is assessed based on the convergence of the multipliers, as shown in table 2. The diagnostic parameters converge to three significant figures or better with $N_p = 7$, the same as in the convergence study of the two-dimensional base flows (table 1), so $N_p = 7$ was adopted for all subsequent Floquet analyses.

The code has been validated against other analyses for the circular and square cylinder wakes (Blackburn & Lopez 2003) and three-dimensional DNS of a swirling axisymmetric flow (Blackburn 2002). For the flow under study here, we can compare directly with the experiments of Vogel *et al.* (2003, figure 17), where the transition from two-dimensional to three-dimensional flows was determined for $St \in [14, 53]$. Our computed critical locus for the onset of three-dimensional instability is shown compared to the experimental results in figure 3. The open circles are the experimentally

observed two-dimensional base states and the filled diamonds are the experimentally observed three-dimensional synchronous states. The solid circles and the spline-fitted curve are the locus of the bifurcation points from two-dimensional to three-dimensional mode B synchronous states, as predicted by the Floquet analysis. The agreement is in general very good, considering the finite spanwise extent of the cavity used in the experiments.

4. Stability of the basic state

When Re is increased beyond a critical value (that depends on St), the two-dimensional basic state undergoes symmetry-breaking bifurcations leading to three-dimensional states with periodic structure in the z-direction. Depending on St, we have found that the basic state undergoes either synchronous or Neimark–Sacker bifurcations. We have found two distinct synchronous modes that have some similarities to the synchronous modes A and B that bifurcate from the two-dimensional periodic shedding state in the wake of a circular cylinder. We have chosen to also refer to our synchronous modes as A and B, and to the new quasi-periodic mode as QP.

In the two-dimensional (St, Re) control space there are three distinct loci along which the different modes reach criticality, i.e. along which $|\mu| = 1$ for some value of spanwise wavenumber β. Figure 4 shows variations of the moduli of Floquet multipliers, $|\mu|$, with the spanwise wavenumber, β, at three different pairs of the control parameters (St, Re). Each of the pairs (St, Re) corresponds to an example for the onset of three-dimensional flow via each of the three types of modes, A, B and QP. In these examples, the critical spanwise wavelength for mode A is $\lambda/h \approx 2\pi/1.7 = 3.7$, which is much greater than that for either mode B or QP, both with $\lambda/h \approx 2\pi/8.5 = 0.74$ at these values of (St, Re). For comparison, the wavelengths of modes A and B for the cylinder wake at onset are approximately 4.0 and 0.82 cylinder diameters, respectively (Barkley & Henderson 1996).

The variation with St of the spanwise spatial scales associated with each of the three modes is illustrated in figure 5. In this figure, the variation of $|\mu|$ with β is presented over a range $St \in [10, 200]$ at the critical Re for each value of St; the three thick lines indicate critical loci for each of the three modes as labelled, where $|\mu| = 1$. The critical spanwise wavelengths for the three modes are quite distinct; mode A has the largest wavelength, mode B the shortest, and mode QP has wavelengths intermediate between those of modes A and B.

The bifurcation curves for the three modes in (St, Re)-space are presented in figure 6(a). At low St, mode B is the first to become critical with increasing Re; at high St, mode A is first, and at intermediate St ($St \in [87.5, 132]$), mode QP becomes critical first. In figure 6(b), the corresponding critical wavenumbers are plotted; this figure represents the projection of the three-dimensional stability surface (figure 5) onto the two-dimensional (St, β)-plane. It is interesting that the wavenumbers for the onset of mode QP are approximately the same as for mode B at low St, and also that at $St = 87.5$, where the mode B and mode QP bifurcation curves intersect, the wavenumber for mode B is approximately double that for mode QP. Beyond approximately $St = 40$, β_c for mode B increases almost linearly with St, until it reaches $\beta_c = 2\pi h/\lambda_c \approx 14.5$, i.e. until the wavelength of the spanwise periodicity is reduced to approximately the radius of the spanwise roller.

A comparison of the bifurcation curve of mode B in (St, Re)-space with experimental observations of the base state and mode B state from Vogel *et al.* (2003) was shown previously in figure 3. The fact that the agreement was quite good is an indication

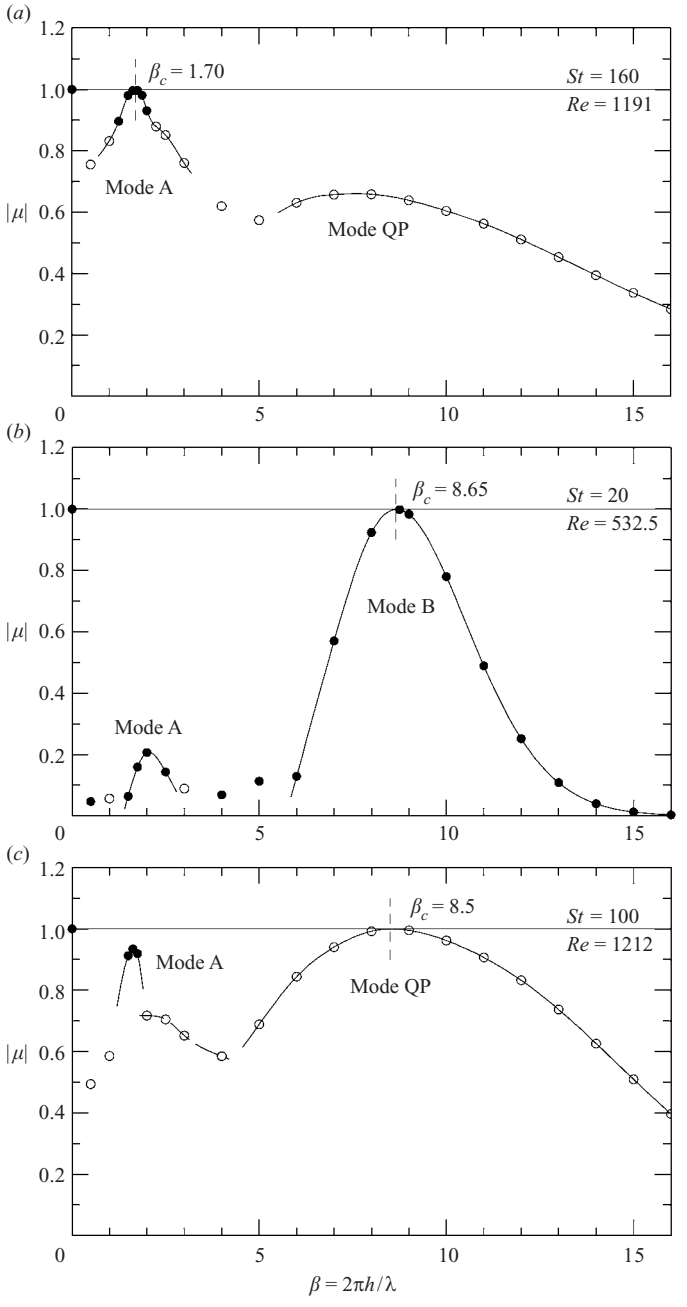

FIGURE 4. Modulus of the Floquet multipliers, $|\mu|$, as a function of the spanwise wavenumber, β, at critical Re for three sample St, corresponding to the different modes: (*a*) mode A at ($St = 160$, $Re = 1191$), (*b*) mode B at ($St = 20$, $Re = 532.5$), and (*c*) mode QP at ($St = 100$, $Re = 1212$). Filled circles indicate real Floquet multipliers, open circles indicate the occurrence of complex-conjugate pairs.

that the onset of mode B is via a supercritical bifurcation; this point will be taken up again in § 5.4. We can also compare with measurements of wavenumber for mode B from the same set of experiments. In figure 6(*b*), the value of β from figure 14 of

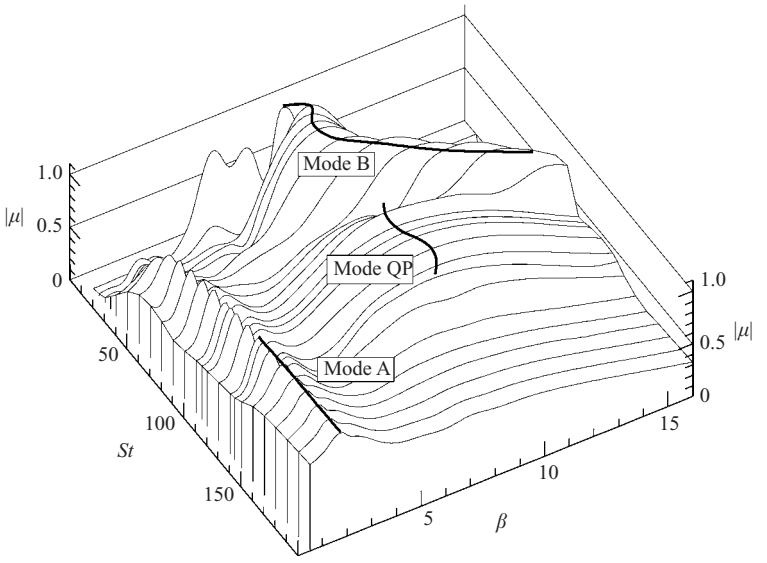

FIGURE 5. The variation of $|\mu|$ with $\beta = 2\pi h/\lambda$ over a range $St \in [10, 200]$ at the critical Re for each value of St; the three thick lines indicate the loci where $|\mu| = 1$, each thick line corresponding to criticality of one of the three modes.

Vogel *et al.* (2003), extrapolated to $Re_c = 835$ at $St = 53$, is seen to fall almost exactly on the value predicted by the Floquet analysis.

In the following two sections we summarize the symmetries and characteristics of the unstable modes, based on both Floquet analysis and full DNS results near the onset of instability for the three modes, based on specimen results computed at set values of St. Modes A and B, computed at $St = 160$, 20, respectively, are dealt with in § 5, while mode QP, computed at $St = 100$, is described in § 6.

5. Spatio-temporal structure of the synchronous modes

Following the common usage for descriptions of mixing-layer and wake flows, the terms 'roller' and 'braid' denote, respectively, large-scale rotating flow structures with primarily spanwise-aligned vorticity, and smaller-scale structures that can be visualized using vorticity components that are orthogonal to the spanwise direction. Braid-like structures are typically spanwise-orthogonal perturbation vorticity that is amplified through stretching induced by the primary flow.

The two three-dimensional synchronous modes have cellular flows. This is clearly seen from the structure of their eigenfunction expansions, as detailed in § 2. The velocity in the spanwise direction, w, is zero at $z = n\lambda/2, \forall n \in \mathbb{I}$ and $\forall t$, implying zero flux across the nodal planes. The two modes A and B are three-dimensional T-periodic standing waves.

5.1. *Basic states*

Instantaneous contours of spanwise vorticity at $T/8$ phases illustrating the basic states that are unstable to modes A and B are shown in figure 7. At times $t = 0$ and T, the cavity floor is at rest, about to begin moving in the $+y$-direction. Both basic states exhibit large spanwise rollers located at the $\pm y$ ends of the cavity.

The most obvious distinguishing feature of the basic state that is unstable to mode A (figure 7*a*) is the persistence of two strong rollers through all phases of the

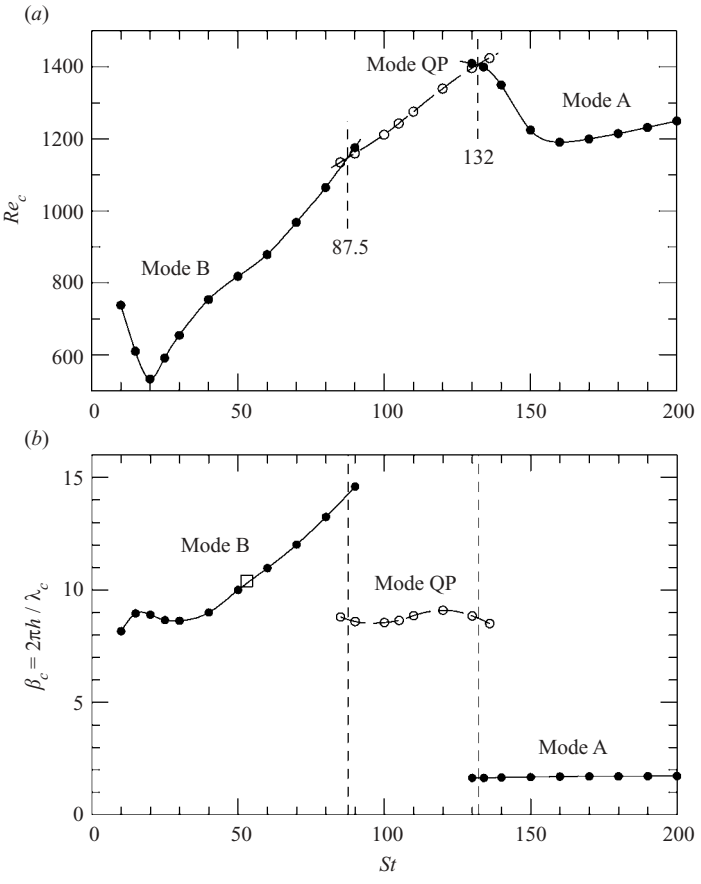

FIGURE 6. Plots of the critical values of (*a*) *Re* and (*b*) β, as functions of *St*, for the transition from the two-dimensional basic state to the three-dimensional states, modes A, B and QP. Closed (open) circles are used to represent solution branches with real (complex-conjugate pair) Floquet multipliers. In (*b*), □ represents the value of β at $St = 53$ from the experiments of Vogel *et al.* (2003, figure 14), extrapolated to $Re_c = 835$.

floor cycle. In contrast, for the basic state that is unstable to mode B, it can be seen in figure 7(*b*) that at $2T/8$ and $6T/8$ there is essentially only a single roller present. A less obvious distinction is the fate of shear layers that form on the vertical walls of the cavity, i.e. at $y = \pm h$. For base states unstable to mode B, these shear layers wrap around and are stretched by the roller adjacent to the wall producing the shear layer; the shear layer and the roller have opposite signed vorticity. For base states unstable to mode A, however, the corresponding shear layers separate from the vertical walls and penetrate into the core of the roller adjacent to the shear-layer-producing wall; again, the shear layer and the roller have opposite signed vorticity. There is a smooth continuum of basic states for *St* and *Re* intermediate for those of figure 7(*a*, *b*). Additional contour plots corresponding to other basic states that are unstable to mode B may be found in Vogel *et al.* (2003).

5.2. *Perturbation enstrophy of the synchronous modes*

Instantaneous contours of enstrophy (the magnitude of vorticity) associated with the critical Floquet eigenfunctions of the base flows shown in figure 7, are plotted

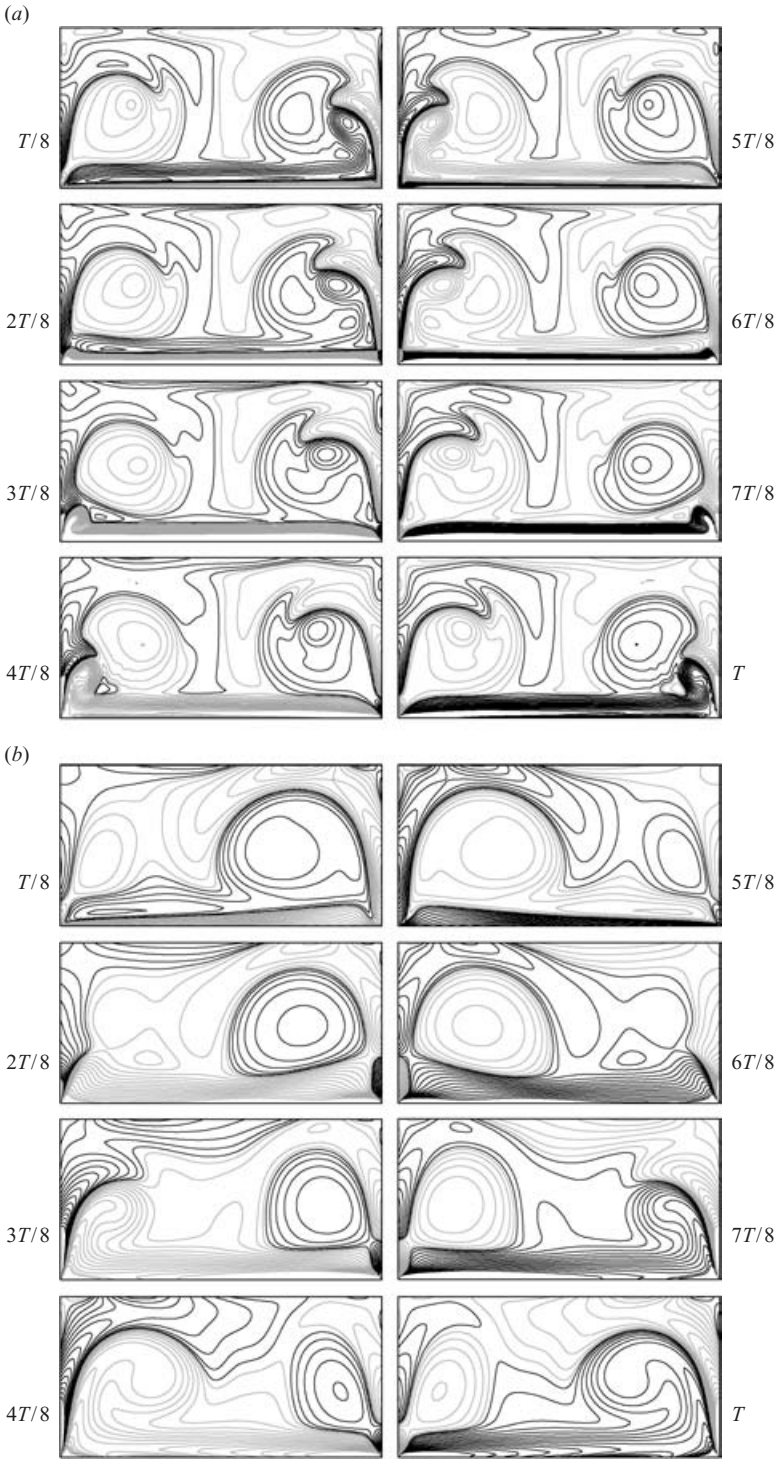

FIGURE 7. Contours of z-vorticity of the basic state at (a) ($St = 160$, $Re = 1191$) which is marginally unstable to mode A, and (b) ($St = 20$, $Re = 532.5$) which is marginally unstable to mode B, at $T/8$ phases over one forcing period. In each panel, the cavity floor is at the bottom. Black/grey contours represent positive/negative vorticity.

in figure 8. These enstrophy contours are shown on planes $z = \lambda_c/4 + n\lambda_c/2, n \in \mathbb{I}$. These are planes on which the x and y components of perturbation vorticity have extrema – the z component, however, has extrema at $z = n\lambda_c/2$. An H-symmetry of the perturbation enstrophy – a non-negative scalar quantity – is apparent.

By comparison with figure 7(a), it can be observed that for mode A instability (figure 8a), the largest perturbation enstrophy is located on the walls and within the cores of the rollers. In contrast, for mode B, the perturbation is strongest in the shear layers that wrap around the roller, and there is little evidence of significant perturbation within the core of the single roller that is present at any time. The vortex-core perturbation enstrophy appears to be continuously present within each roller for mode A, and replenished with each floor stroke. The perturbation enstrophy for mode B appears to be essentially regenerated anew with each stroke. Further, it is apparent that this enstrophy is absorbed into the Stokes layer and wrapped around the roller at the opposite end of the cavity during the second half of the cycle, providing a seed for the perturbation enstrophy in the succeeding stroke of opposite sense.

5.3. *Three-dimensional structure and symmetries of the synchronous modes*

The three-dimensional structures of modes A and B are visualized with the aid of perspective views of instantaneous vorticity isosurfaces in figure 9. The left-hand column of the figure illustrates the critical Floquet eigenfunctions for modes A and B ($St = 160$ and 20, respectively), while the right-hand column illustrates very similar asymptotic results from DNS at the same St and β values, but at slightly elevated (supercritical) Re.

In all panels of the figure, translucent isosurfaces show the spanwise component of vorticity, and solid isosurfaces show the vertical component of vorticity (which is analogous to the streamwise component of vorticity in a bluff-body wake). It should be noted that in the case of the Floquet eigenfunctions, the spanwise (translucent) vorticity does not correspond to the eigenfunction, but to the two-dimensional DNS of the base flow at the same phase in time; this combination is used to emphasize the spatio-temporal relationship between the perturbation and the base flow. However, for isosurfaces illustrating the saturated DNS, the spanwise and vertical vorticity both come from the same three-dimensional nonlinear simulation.

For mode A, there is significant vertical perturbation vorticity at all times both within and between the spanwise rollers, as well as on the vertical walls of the cavity. The combination of vorticity isosurfaces employed does not directly illustrate the spanwise perturbation vorticity for mode A, but in fact this component is very significant in comparison with the vertical vorticity component, and resides largely within the cores of the rollers. The contribution of the spanwise perturbation component is however reflected in the waviness of the rollers, which can be seen in the DNS results of figure 9(b). Note that the wave shape of each roller stays essentially fixed in space at phases t_0 (the time at which the floor reaches its maximum travel in the $-y$-direction) and $t_0 + T/2$, and that the extrema in the perturbation x-vorticity maintain their orientation throughout the cycle.

For mode B, the dominant perturbation x-vorticity resides in braids within the shear layers wrapped around the rollers, as is clearly marked by the isosurfaces of perturbation x-vorticity in figure 9(c, d). In comparison to mode A, note that (i) for mode B the cores of the rollers do not become significantly wavy and (ii) the perturbation x-vorticity at a given spanwise and y-location changes sign as time proceeds from t_0 to $t_0 + T/2$.

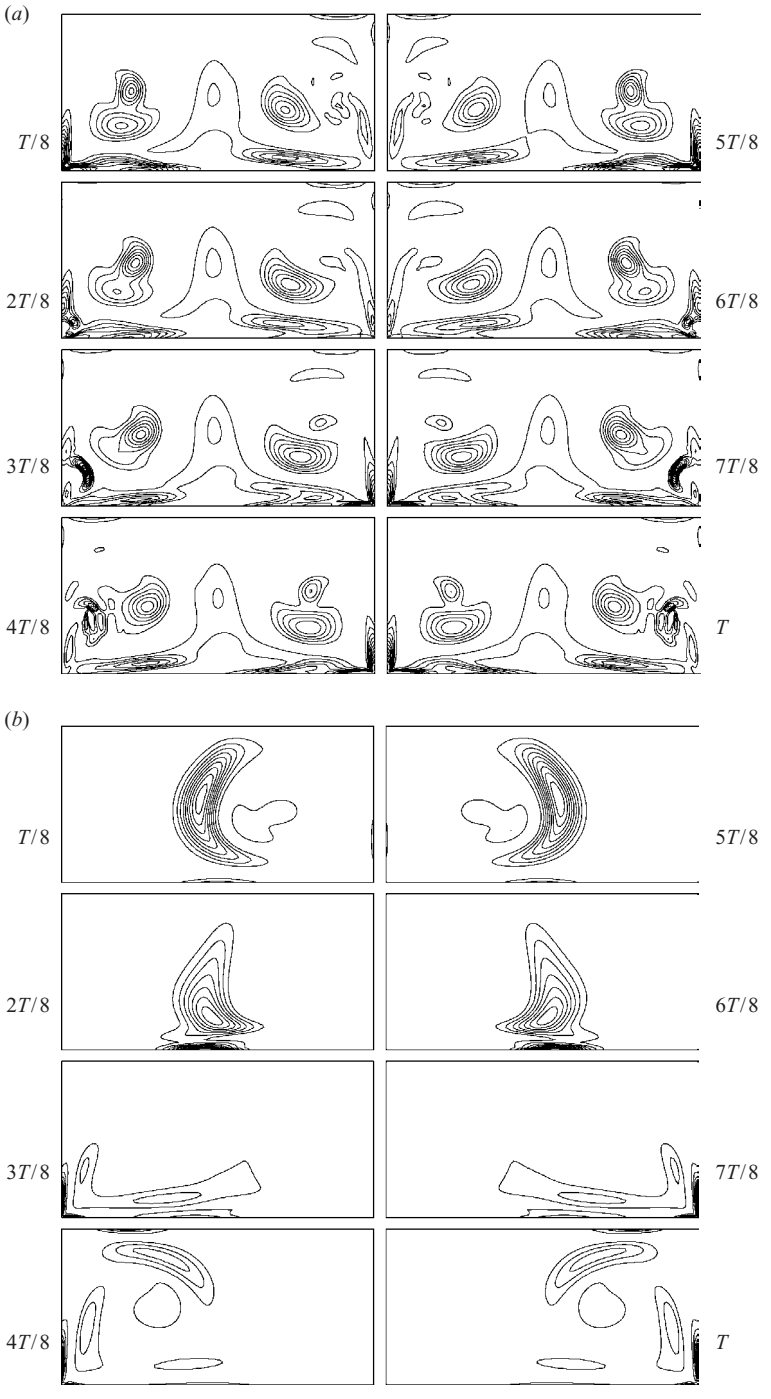

FIGURE 8. Contours of the enstrophy of (*a*) the mode A Floquet eigenfunction at ($St = 160$, $Re = 1185$), and (*b*) the mode B Floquet eigenfunction at ($St = 20$, $Re = 532.5$), over one forcing period, T. The data are extracted at $z = \lambda/4$, where the x, y components of vorticity have extrema.

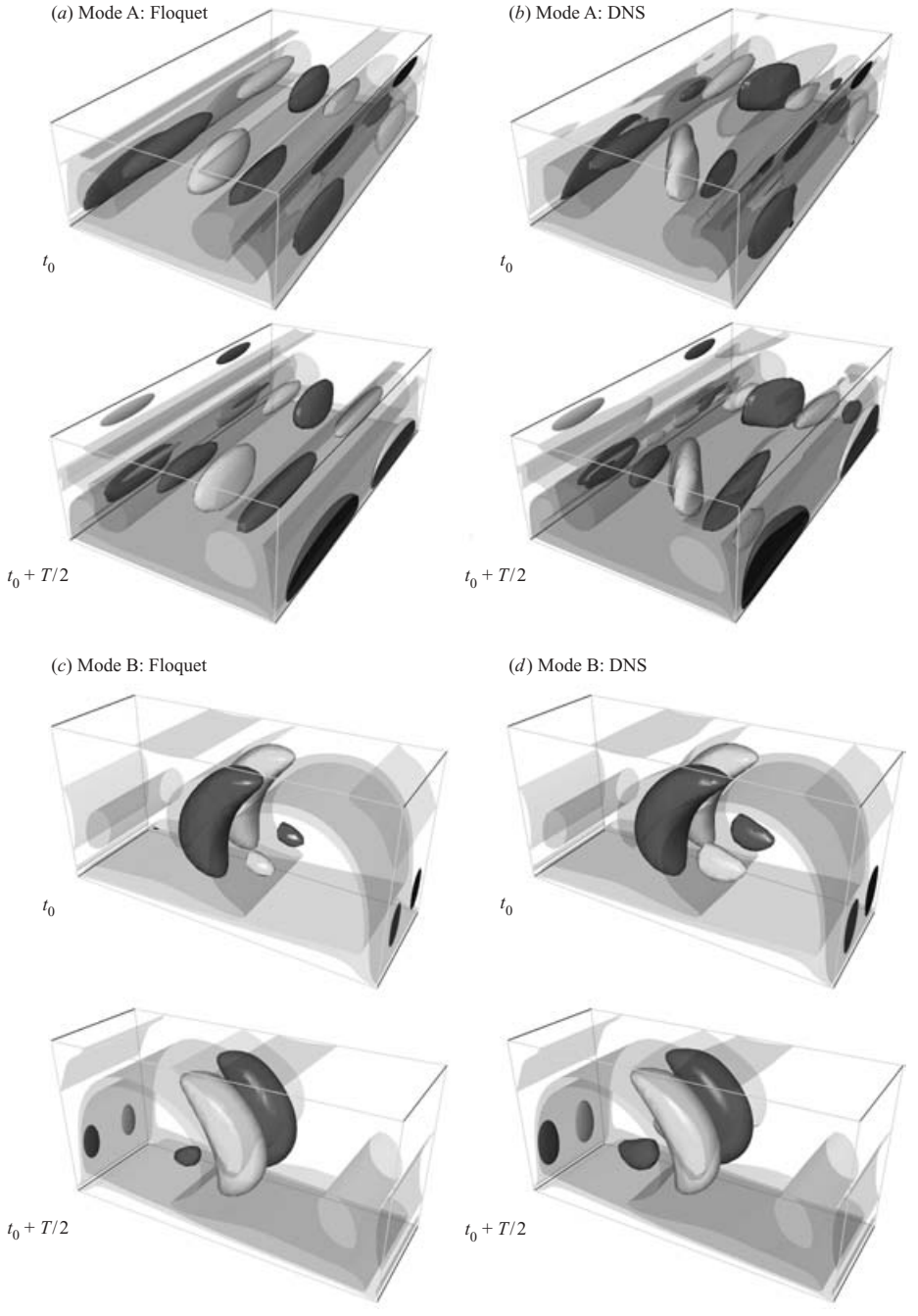

FIGURE 9. Comparisons of instantaneous vorticity isosurfaces from Floquet analysis with those from direct numerical simulation for mode A at $St = 160$ and $\beta = 1.7$, and mode B at $St = 20$ and $\beta = 8.75$, at two times t_0 and $t_0 + T/2$. In all panels, solid isosurfaces represent x-component and translucent isosurfaces represent z-component vorticity. Results in (*a*) show the x-vorticity of the Floquet eigenfunction against the vorticity field of the base flow at $Re = 1191$; those in (*b*) show x- and z-vorticity both from the saturated nonlinear state at $Re = 1250$; (*c*) those in show the y-vorticity of the Floquet eigenfunction against the vorticity field of the base flow at $Re = 532.5$; those in (*d*) show x- and z-vorticity both from the saturated nonlinear state at $Re = 535$.

By examining the three-dimensional structure of the velocity field associated with modes A and B over a forcing period, it is found that mode B preserves H-symmetry:

$$(u, v, w)(x, y, z, t) = (u, -v, w)(x, -y, z, t + T/2), \tag{5.1}$$

whereas mode A breaks H-symmetry, but is invariant to another space–time symmetry:

$$(u, v, w)(x, y, z, t) = (u, -v, w)(x, -y, z + \lambda/2, t + T/2). \tag{5.2}$$

This new space–time symmetry consists of the H-symmetry composed with a spanwise translation of one-half wavelength. These are the only two options for velocity vectors of three-dimensional T-periodic modes.

It is instructive to compare the present long and short wavelength synchronous modes with those of the cylinder wake flows. The general shape and alignment of the perturbation x-vorticity for mode B has many similarities to what is seen in the streamwise (x) perturbation vorticity for cylinder wakes. Both are braid-type shear-layer instabilities, aligned predominantly normal to the base flow. The instability produces comparatively little change in the spanwise vorticity of the main rollers. In both flows, mode A, in contrast, brings about comparatively large changes in the spanwise vorticity of the main rollers, which become observably wavy as a result – the perturbation vorticity is significant within the main rollers. The space–time symmetries of our modes A and B (equations (5.1)–(5.2)) are opposite those of the cylinder wakes (e.g. see Robichaux *et al.* 1999; Barkley, Tuckerman & Golubitsky 2000; Blackburn & Lopez 2003); the wake long-wave mode A and our short-wave cavity mode B both preserve H-symmetry, whereas the short-wave wake mode B and our long-wave cavity mode A break H-symmetry, but are invariant to another space–time symmetry, (5.2). We will return to these points in § 7.1.

5.4. *Nonlinear stability analysis of synchronous modes*

The nonlinear criticality of the synchronous bifurcations to three-dimensional modes A and B is determined by examining the variation with Reynolds number of a measure related to the energy (squared amplitude) of the instability modes, obtained using three-dimensional DNS. This measure of the perturbation energy is

$$q_z = \frac{1}{4V_{max}^2 \Gamma h^2 \lambda} \int_0^h \int_{-\Gamma h/2}^{\Gamma h/2} \int_{-\lambda h/2}^{\lambda h/2} \langle w^2 \rangle \, \mathrm{d}z \, \mathrm{d}y \, \mathrm{d}x, \tag{5.3}$$

i.e. q_z is the normalized contribution to the time-averaged kinetic energy from the spanwise velocity component, which is zero for the base state. Figure 10 shows how q_z varies with Re for modes A and B, over a small range of Reynolds numbers above Re_c. Here, Re_c is derived from the Floquet analysis at the same St. The spanwise wavelength λ used in the DNS likewise derives from the critical Floquet mode, as does the small perturbation applied to the base flow used to initialize the three-dimensional DNS.

For a supercritical pitchfork bifurcation, we expect the squared amplitude of the perturbation (and q_z) to initially show linear growth with $|Re - Re_c|$. This is clearly the case in figure 10(b), immediately identifying the bifurcation to mode B as being of supercritical type. The situation for mode A (figure 10a) is more complicated. Here, it can be seen that $q_z \sim |Re - Re_c|^{1/2}$ – this is again a supercritical pitchfork bifurcation, but close to a degenerate case in which the first Landau constant (Drazin & Reid 1981) is effectively zero and the growth to saturation is governed by the second Landau constant (coefficient of the quintic terms in perturbation amplitude), which is positive. These results have been confirmed by analyses of the temporal growth

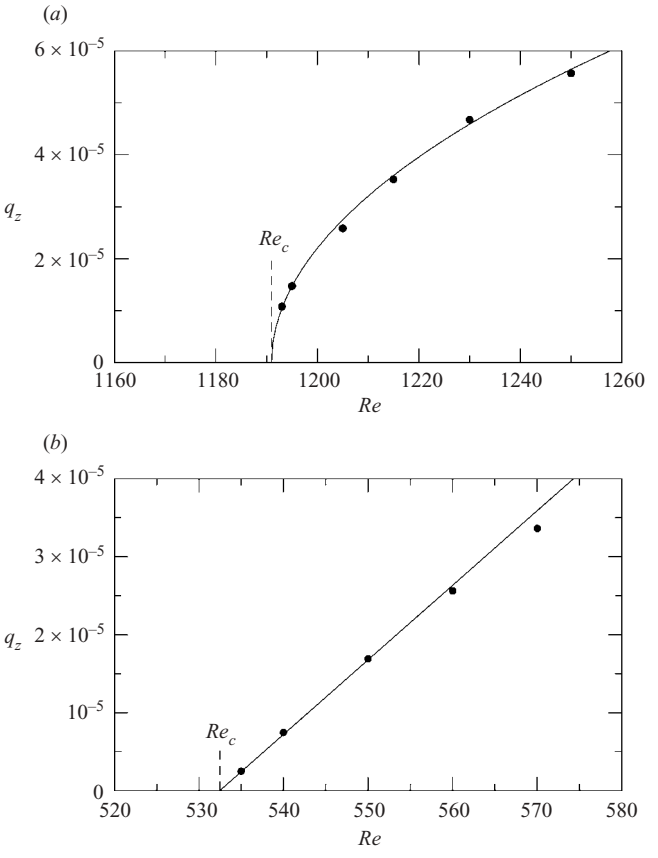

FIGURE 10. Analysis of the nonlinear energy growth with departure from critical Reynolds number, Re_c for (*a*) mode A at $St = 160$ and (*b*) mode B at $St = 20$. The ordinate, q_z, is a measure of the contribution of the three-dimensional instability to the total kinetic energy. Each mode exhibits a different kind of supercritical bifurcation: mode B is a standard supercritical bifurcation, but mode A is partially degenerate, with a near-zero first Landau constant.

to saturation (not shown): for both modes A and B, the growth of the perturbation energy does not exceed exponential, and in the case of mode A, the saturation is fitted best by quintic terms, any contribution from cubic terms being negligible.

The corresponding weakly nonlinear analyses for the synchronous modes of the cylinder wake shows that the short wavelength mode B is supercritical and the long wavelength mode A is subcritical (Henderson & Barkley 1996; Henderson 1997), i.e. the first Landau constant for mode A is small and negative. The synchronous bifurcation producing mode A in the driven cavity flow does not necessarily remain slightly supercritical along its entire bifurcation curve (a point we have not checked), as the Landau constants vary with parameters and it is quite possible that the bifurcation could also become subcritical at some point on the curve.

6. Spatio-temporal structure of the quasi-periodic mode

6.1. *Basic states*

The form of the base state which is unstable to mode QP has characteristics in common with those of the base states that are unstable to modes A and B; figure 11

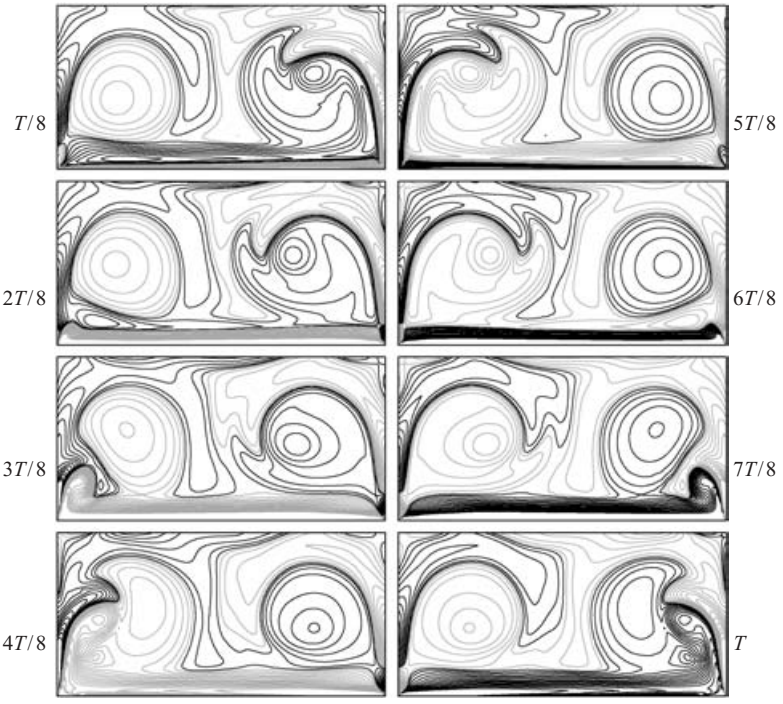

FIGURE 11. Contours of z-vorticity of the basic state at ($St = 100$, $Re = 1212$) (which is unstable to mode QP) over one forcing period, T.

shows contours of the z-vorticity of the basic state at $St = 100$, $Re = 1212$ over one forcing period, T (cf. figure 7). It is apparent that there are two rollers during the entire cycle, as for the base states that are unstable to mode A, but they have more variability over the cycle. Basic states that are unstable to mode B exhibit more variability in the size of the rollers as the roller at each end of the cavity dissipate completely over part of the cycle. The shear layers that form on the vertical walls of the cavity tend to penetrate and disrupt the roller adjacent to that wall (which has vorticity of the opposite sign of that in the shear layer), as with base states unstable to mode A (see figure 7*a*). However, a strong uninterrupted shear layer also envelopes that roller (e.g. at times $t = 3T/8$ to $t = 5T/8$), as is the case with basic states unstable to mode B.

6.2. *Floquet analysis: secondary periods and wave speeds*

The onset of the quasi-periodic states occurs when complex-conjugate pairs of Floquet multipliers cross the unit circle: $\mu = e^{\pm i\theta}$. The bifurcation introduces a secondary period related to θ: $T_s = 2\pi T/\theta_{sr}$, where θ_{sr} is a self-rotation, or winding, number. Floquet analysis based on the Poincaré map does not necessarily provide the self-rotation number, but rather an angle $\theta \in [0, \pi]$. The relationship between θ and θ_{sr} is $\theta_{sr} = 2l\pi \pm \theta$, where the sign and integer multiple l are undetermined. For maps that are derived from continuous systems, there are a variety of methods available to unambiguously determine θ_{sr} from θ (e.g. see Lopez & Marques 2000; Blackburn 2002). Here, we directly determined the second period from the nonlinear quasi-periodic solution, to find $\theta_{sr} = \theta$.

Figure 12(*a*) shows the variation of T_s/T with St. It can be seen that the secondary period T_s reaches a minimum near $St = 105$, and that T_s approaches, but does not quite

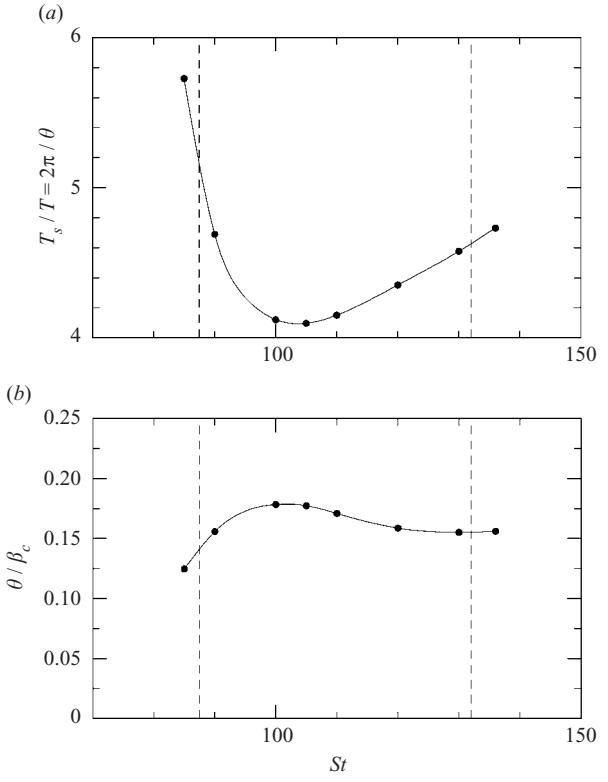

FIGURE 12. (*a*) The ratio of Neimark–Sacker period to floor oscillation period as function of *St* at the critical values of *Re* and β for the onset of mode QP. Mode QP is the first to become critical as *Re* is increased for values of *St* between the dashed lines. (*b*) Dimensionless wave speed as function of *St* at the critical values of *Re* and β for the onset of mode QP.

achieve, a 1:4 subharmonic resonance with the base flow. While the Neimark–Sacker bifurcation is close to a strong resonance (i.e. $T/T_s = p/q\,;\, p, q \in \mathbb{Z}$ with $q \leqslant 4$), we have not encountered locking in the limited set of nonlinear computations that we have run.

At the bifurcation, the $O(2)$ symmetry produces a pair of complex eigenfunctions, each of which correspond to modulated travelling waves ($\pm z$-TW); these can be combined symmetrically to produce a quasi-periodic standing wave (SW). Both TW and SW are modulated by the underlying periodic base flow. The ratio θ/β_c can be interpreted as a dimensionless wave speed, i.e. how far in cavity-height units h a TW will travel in z during one floor period T. Figure 12(*b*) shows the variation of this wave speed with *St*; at onset, all TW travel $\Delta z \approx h/6$ during $\Delta t = T$.

6.3. *Three-dimensional structure and symmetries of the quasi-periodic modes*

Figure 13 shows translucent isosurfaces of z-vorticity with solid isosurfaces of x-vorticity for the critical Floquet modes at ($St = 100$, $Re = 1212$), and for saturated DNS at ($St = 100$, $Re = 1225$), illustrating both TW and SW solutions at phases $T/2$ apart. This figure is analogous to figure 9 for the synchronous modes, and again it is the z-vorticity of the basic state (as opposed to that of the Floquet mode) that is illustrated in the left-hand column, but z-vorticity of the nonlinear solution that is used in the right-hand column.

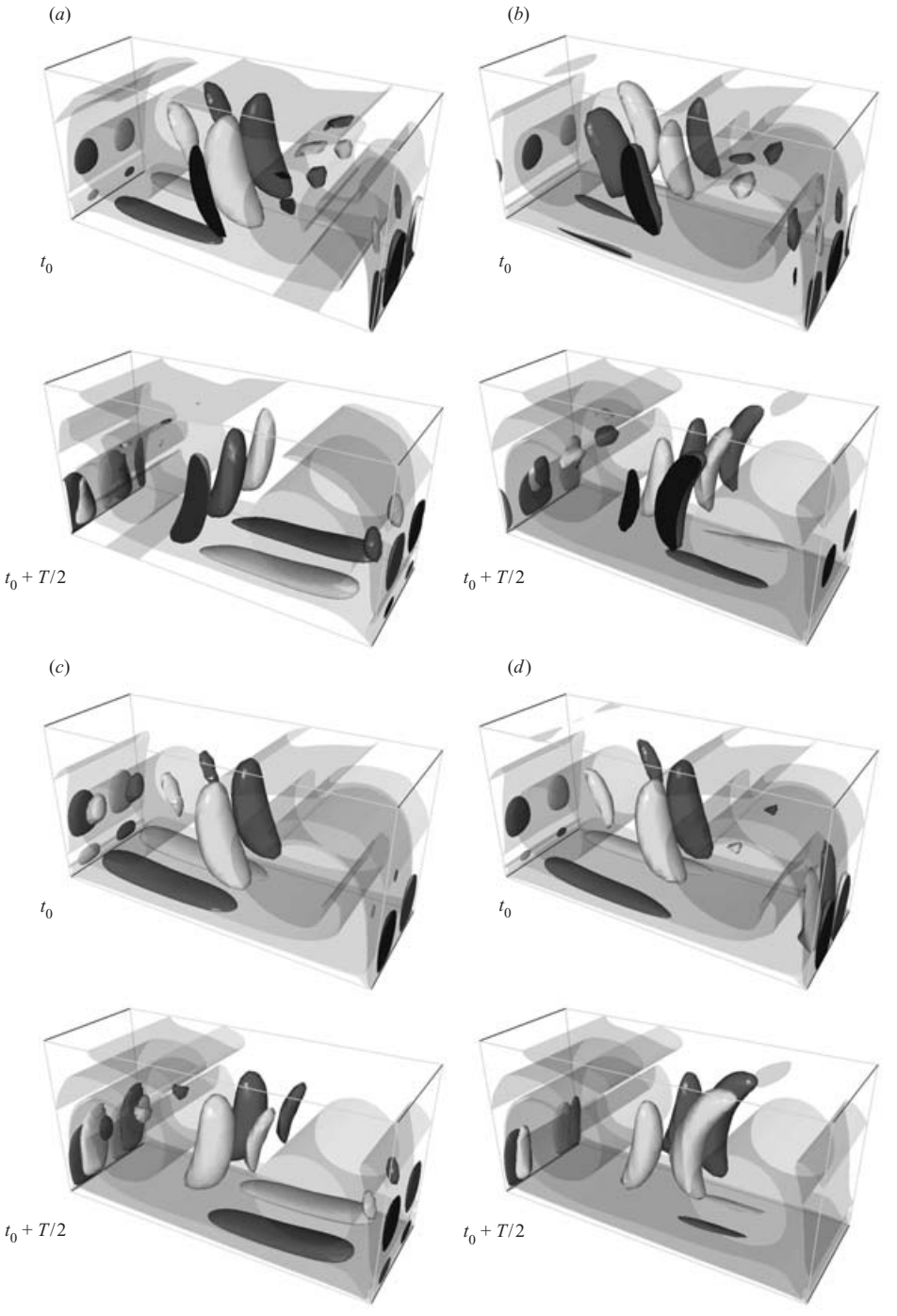

FIGURE 13. Comparisons of instantaneous vorticity isosurfaces from Floquet analysis with those from direct numerical simulation for (a, b) travelling-wave (TW) and (c, d) standing-wave (SW) states for mode QP, $St = 100$ and $\beta = 8.5$, at two times t_0 and $t_0 + T/2$. In all panels, solid isosurfaces represent x-component and translucent isosurfaces represent z-component vorticity. Results in (a, c) show the x-vorticity of the Floquet eigenfunction against the vorticity field of the base flow at $Re = 1212$; those in (b, d) show x- and z-vorticity both from the saturated nonlinear state at $Re = 1225$.

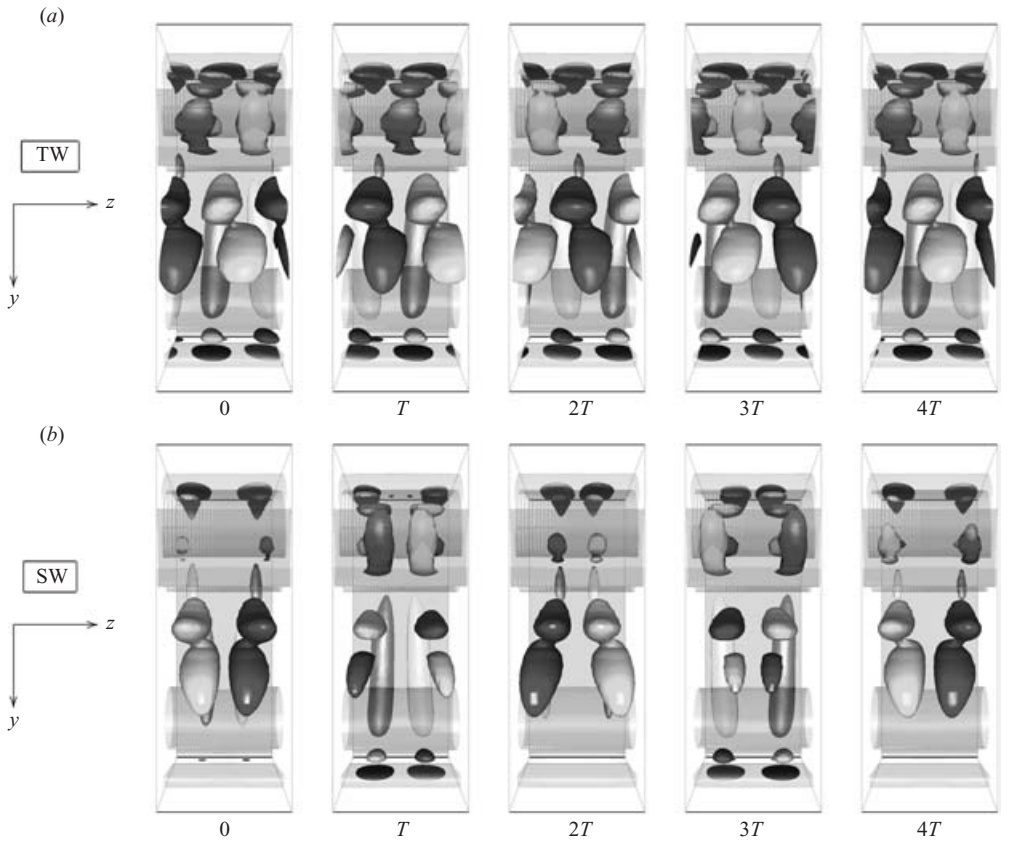

FIGURE 14. Top views (from $+x$) of isosurfaces of vorticity from DNS at ($St = 100$, $Re = 1225$), over four floor cycles for (a) the $+z$-TW and (b) SW. Solid isosurfaces: x-component vorticity; translucent: z-component. The time taken for the passage of the TW through the represented domain (one spanwise wavelength, λ) can be seen to be very close to $4T$ (see figure 12a).

A comparison of figures 9 and 13 suggests that mode QP has more in common with mode B than with mode A, since the dominant features of the perturbation flows again appear to be braid-like shear-layer instabilities. A difference from mode B is that rollers persist at both ends of the cavity throughout the entire floor cycle. For mode QP, the shear layers that wrap around these rollers interact, as do their instabilities (i.e. the braids).

To help illustrate the nature of the TW state, and to compare it with the SW state, figure 14 shows the TW and SW x-vorticity from DNS at ($St = 100$, $Re = 1225$), strobed at the floor oscillation period, over four cycles. Comparing the solutions at times 0 and $4T$, for SW the solutions have very similar structure, but the strengths of the various structures differ; this is due to the modulation implied by the quasi-periodicity. For the TW, on the other hand, the strobed structures remain invariant in a translating frame of reference, and they translate almost one complete wavelength λ in time $4T$. This is consistent with the approximately 4:1 ratio of T_s/T provided by the Floquet analysis at $St = 100$ (see figure 12a).

In order to understand the physics of the mode QP wave states better, figure 15 presents vorticity isosurfaces at $T/6$ phase increments over one floor oscillation cycle. For the TW state, there is considerable organization and regularity. The braids on

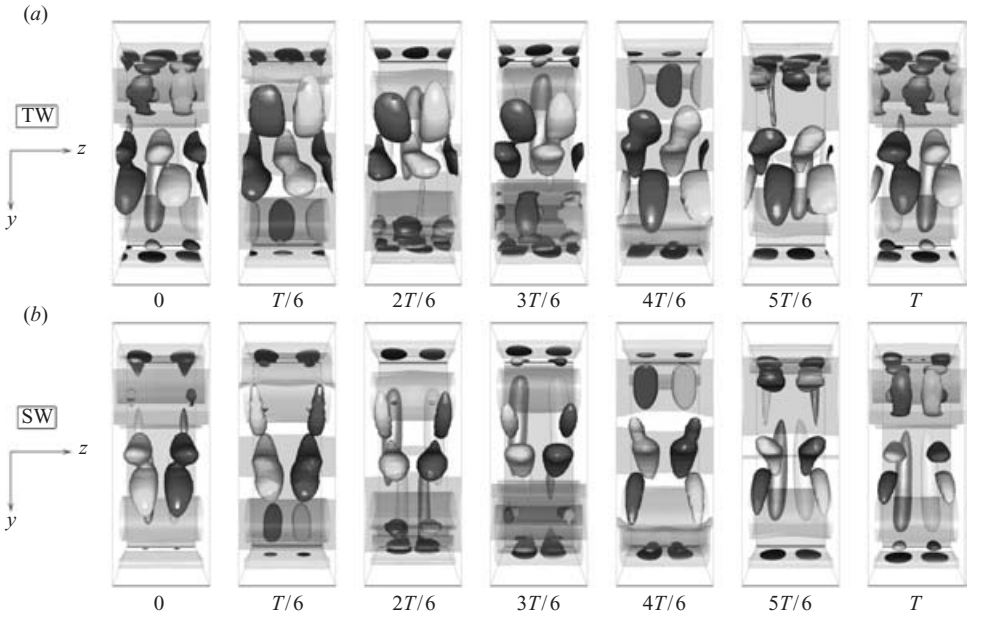

FIGURE 15. Top views (from $+x$) of isosurfaces of vorticity at ($St = 100$, $Re = 1225$), at $T/6$ phases for (a) $+z$-TW and (b) SW. Solid isosurfaces: x-component vorticity; translucent: z-component. For the TW, note the merging of structures of like-signed vorticity, moving in the $+z$-direction as time proceeds.

opposite rollers form, displaced by $\lambda/4$ in the spanwise direction, and for the $+z$ ($-z$) TW state the braids on the 'old' roller are absorbed by like-signed braids at the spanwise location $\lambda/4$ to their $+z$ ($-z$) on the newly formed opposite roller. This merging process, continually repeated, produces a modulated travelling wave. By comparison, the SW state exhibits no regularity, owing to its quasi-periodic nature – there is no reference frame in which the SW state appears periodic. By observing similar sequences for the SW state over much longer periods (not shown), it is seen that at some times, positive x-vorticity braids meet negative x-vorticity braids from the opposite roller, and at other times they meet positive x-vorticity braids; however, as is to be expected for a spanwise reflection-symmetric SW, there is no net spanwise migration of the braids.

The modulated travelling waves break the reflection invariance in z, and so there are two of them, $+z$- and $-z$-travelling, and one is obtained from the other by reflection in z. They retain a discrete translation invariance in z. They also break the space–time H-symmetry, but are invariant to another space–time symmetry corresponding to the H-symmetry operation applied in a frame moving at the wave speed. The quasi-periodic standing waves break the translation invariance in z, so there is a continuous family of these parameterized by their spanwise phase; all members can be generated from one by translations in z. They retain a reflection invariance in z, centred about their nodes. They break the space–time symmetry H and possess no space–time symmetry.

6.4. *Time-average streaming flow of the TW states*

The TW, unlike SW and modes A and B, are not cellular, and as such have a net flux in the spanwise direction ($\pm z$, depending on which direction the wave is travelling).

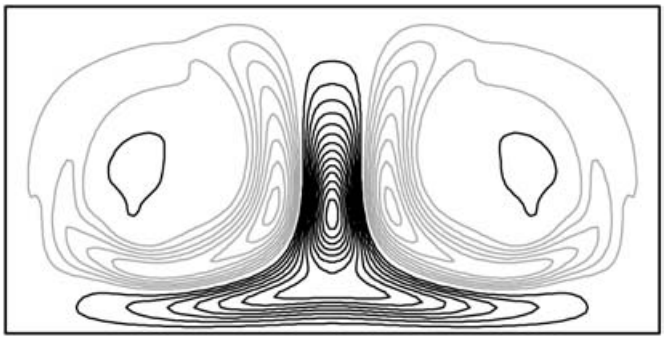

FIGURE 16. Contours of average spanwise velocity for the $+z$-TW at $St = 100$, $Re = 1225$, Black contours represent negative values of w; grey, positive.

For example, at ($St = 100$, $Re = 1225$), the nonlinear $+z$-TW state has a normalized net axial velocity given by

$$\frac{W_s}{V_{max}} = \frac{1}{V_{max} h^2 \Gamma} \int_0^h \int_{-\Gamma h/2}^{\Gamma h/2} \langle w \rangle \, \mathrm{d}y \, \mathrm{d}x = 1.29 \times 10^{-5}, \tag{6.1}$$

i.e. the net axial flux is in the same direction as the motion of the TW, but is quite small. This situation is analogous to that which occurs in Taylor–Couette flow when the basic Couette flow loses stability via a Hopf bifurcation with $O(2)$ symmetry, and either spirals (travelling waves) or ribbons (standing waves) result; the spirals produce a net axial flux, but the ribbons do not (e.g. see Chossat & Iooss 1994; Antonijoan, Marques & Sanchez 1998).

Figure 16 is a contour plot of $\langle w \rangle$ at a z-plane for the $+z$-TW state at ($St = 100$, $Re = 1225$). The black (grey) contours are for positive (negative) velocity. The flow in the positive $+z$-direction is concentrated in the Stokes layer on the oscillating floor and in between the two rollers, near $y = 0$, while the flow in the $-z$-direction is concentrated on the outer edges of the rollers; in the core of the rollers $\langle w \rangle$ is essentially zero. Averaging over the (x, y)-plane gives the value presented in (6.1): a net velocity in the $+z$-direction.

6.5. *Nonlinear stability analysis of the quasi-periodic modes*

The nonlinear criticality of the TW and SW states is examined using the same methodology and diagnostics as was employed for the synchronous modes in § 5.4: the Navier–Stokes solutions are evolved to saturated states at $Re > Re_c$ and the diagnostic q_z is plotted against Re. Here the bifurcations are of $O(2)$-equivariant Neimark–Sacker type as opposed to symmetric pitchforks, but the expected forms of variation of q_z with $|Re - Re_c|$ are the same, and a linear variation signals a supercritical bifurcation. The results for the TW and SW states at $St = 100$ for $Re > Re_c$ are shown in figure 17; both states simultaneously bifurcate supercritically at Re_c, but the TW states have larger energies.

This behaviour is analogous with the theory of Hopf bifurcations with $O(2)$ symmetry (e.g. Golubitsky *et al.* 1988), where both SW and TW bifurcate simultaneously as a result of the symmetry, and a stable solution exists only if both branches bifurcate supercritically. Further, the theory says that the solutions on the branch with largest energy are stable. By subjecting both the saturated SW and TW states to small ($O(10^{-3})$) random perturbations, we have found that the TW states are stable, while the SW states make a transition to one of the two TW states. Since the SW states are

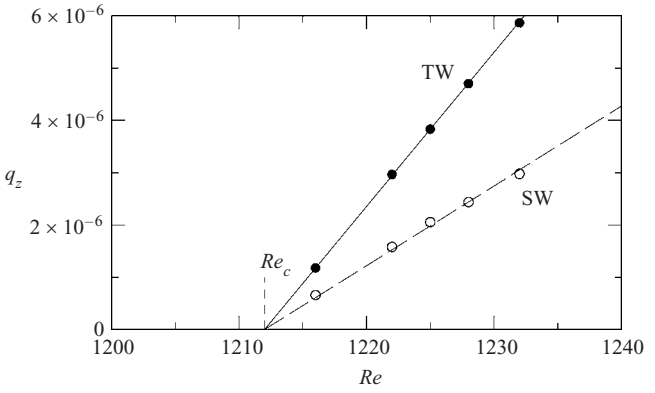

FIGURE 17. Average energy of the spanwise velocity component of TW and SW nonlinear states versus Re at $St = 100$. SW states are unstable to small asymmetric perturbations.

unstable, they cannot be observed as saturated states in physical experiments; the fact that we are able to observe them here stems from the simulations being confined to an invariant subspace by the choice of symmetric initial three-dimensional perturbations to the base flows, and a numerical method that preserves such a subspace.

7. Discussion and conclusions

7.1. *Physical instability mechanisms*

The physical mechanisms leading to the synchronous three-dimensional instabilities of our basic states have much in common with other flows where the basic state consists of rollers aligned in the homogeneous 'spanwise' direction. The analogy is strongest for the periodically shedding wakes of bluff bodies, since the two-dimensional base flows share many of the same physical features and have the same symmetries. A common feature of these flows is the presence of two distinct types of three-dimensional synchronous instability; a roller-core instability, which produces waviness of the rollers, and a shear layer instability, which produces braid-type structures that tend to lie in directions orthogonal to the roller cores. The spanwise lengthscale of the roller-core instability is typically greater than that of the shear-layer instability, which is most probably directly related to the fact that the roller characteristic length (diameter) is usually greater than the shear-layer characteristic length (thickness). A discussion of these types of instabilities, particularly as they apply to cylinder wakes, may be found in Williamson (1996). For the wakes, the critical wavelength λ_c is determined by a single value of Re, Re_c; whereas in the cavity, λ_c and Re_c vary with St. Mode A is a core instability mode and the core diameter is determined by h, not by St, and so λ_c does not vary much with St. On the other hand, mode B seems likely to be a centrifugal instability of the shear layer wrapped around the rollers (on the basis of analysis for the steady driven cavity, see e.g. Albensoeder, Kuhlmann & Rath 2001), and this shear layer originates as the Stokes layer on the oscillatory floor. The thickness of this layer varies with St and as a result so does λ_c. It should also be noted that even longer-wavelength modes exist in open flows (e.g. Crow 1970), but these have significantly different properties to those for the present long-wavelength mode, are not observed either for bluff-body wakes or in the present problem, and will not be further discussed here.

As noted in § 5.3, in the present flow it is mode A, the long wavelength mode, that breaks the H-symmetry of the basic state, while for the wakes of the circular and square cylinders, it is mode B. Owing to the observed physical similarities between the long and short wavelength modes of the wakes and oscillatory cavity flow instabilities, it seems likely that the corresponding modes stem from the same physical instability mechanism in each of the flows. Hence, there is no correlation between physical instability mechanism and the resulting space–time symmetry.

7.1.1. *Synchronous mode A*

The synchronous roller-core instability, mode A, here generates a spanwise wavelength, $\lambda_A \approx 3.7h$, which is comparable to the cylinder-wake roller-core mode, for which $\lambda \approx 4.0D$ at onset. In the present flow, the pair of roller cores for mode A exhibit the same quasi-steady large-scale waviness as observed for an isolated pair of vortices in the work of Leweke & Williamson (1998). When viewed from directions orthogonal to the cavity floor (from $\pm x$), the waviness of the cores in the y-direction is in-phase at all times; when viewed from directions orthogonal to the vertical cavity walls (from $\pm y$), the waviness of the cores in the x-direction is out-of-phase at all times. This pairing of phase relationships (which are independent of the H symmetry (5.2)) is a kinematic rather than dynamic requirement, as pointed out by Leweke & Williamson. The mode A instability of the bluff-body wakes has a similar time-invariant wave-phase pairing.

For quasi-steady problems in which unsteady shear-layer interaction with roller cores is not significant, and where flows are well characterized as initially approximately circular or elliptic vortices with closed streamlines, embedded in a strain field, a consensus has emerged that elliptic instability is the driving mechanism (e.g. Pierrehumbert 1986; Bayly 1986; Landman & Saffman 1987; Waleffe 1990; Leweke & Williamson 1998; Kuhlmann, Wanschura & Rath 1998; Laporte & Leweke 2002). For near-wake flows, which are highly unsteady, and where vortices are significantly distorted by the shear layers that feed them, the situation is more complicated, and it is not yet clear that elliptic instability is necessarily the primary mechanism. Some of the arguments, for and against, are presented by Thompson, Leweke & Williamson (2001).

In regard to the issue of assessment of elliptic instability, the present flow shares some of the complexity of the near-wake flows of the two-dimensional bluff bodies. The base flows that give rise to mode A are unsteady, and the rollers are periodically distorted by the shear layers which penetrate into them and feed them vorticity. Our efforts, not described here, to analyse the localized elliptic instability growth rates (as Thompson *et al.* 2001) have been inconclusive, as the highest growth rates arise in the near-wall shear layers, not within the cores of the rollers. As a result of the strong disruption caused by the regular penetration of the shear layers, it is also difficult to find clear-cut evidence within the rollers of the kinds of perturbation vorticity patterns described by Waleffe (1990) for elliptic instability. On the other hand, the perturbation vorticity is strong within the main rollers and makes them significantly wavy.

7.1.2. *Synchronous mode B*

For the generation of mode B, the perturbation enstrophy evolves on the endwalls ($y = \pm h$) and the top wall ($x = h$), forming an extended shear layer that is swept into the interior of the cavity by the roller that it partially surrounds. This has features in common both with shear-layer roll-up in the near-wake of bluff bodies, and with

steady lid-driven cavity flows. The three-dimensional instability of the shear layer in our flow also appears to have much in common with these other flows. Several studies have investigated the Taylor–Görtler type secondary instabilities of steady lid-driven cavity flows (e.g. Ramanan & Homsy 1994; Albensoeder *et al.* 2001; Migeon 2002). In wake flows, the mechanism for initiation of the instability and spanwise length scale selection has not, to our knowledge, been conclusively determined – while vortex stretching at the saddle/hyperbolic points between the main rollers will amplify any three-dimensional perturbation, this does not select any particular transverse length scale.

In the present flow, the origin of the braid-type three-dimensional features typical of mode B appears to be a centrifugal instability, as for the steady lid-driven cavity flows. And by extension, it is possible that the mode B instabilities in wake flows are also centrifugal in nature. The analytical methods for making this kind of classification, originally developed by Rayleigh for inviscid flows with circular streamlines, were extended by Bayly (1988) to encompass two-dimensional steady flows. More work is needed in order to further extend the method to deal with two-dimensional time-periodic flows before a completely categorical assessment can be made.

7.1.3. *Quasi-periodic mode QP*

The quasi-periodic mode is a novel three-dimensional instability leading to stable modulated travelling waves. Modes with complex-conjugate Floquet multipliers were reported by Barkley & Henderson (1996) for the cylinder wake flow at Re intermediate between modes A and B, but these did not reach criticality, and mode shapes were not presented or discussed. More recently, it has been shown (Blackburn & Lopez 2003) that both the circular and square cylinder wakes have quasi-periodic modes, with wavelengths intermediate between those for modes A and B.

Many of the features of mode QP flows are similar to those of mode B, and hence the underlying mechanism is also likely to be centrifugal instability. While we have presented and discussed both SW and TW states for this mode, the SW state is an unstable state for the parameter regime investigated. The manner in which TWs propagate in the spanwise direction is a result of the merging of braid vortices of like sign that originate as Taylor–Görtler type instabilities, displaced $\lambda/4$ apart in the spanwise direction from opposite ends of the cavity. The TWs generate a net spanwise flux in the same direction as that of wave propagation.

7.2. *Summary*

We have presented stability analysis of a T-periodic two-dimensional flow that shares the symmetries of the two-dimensional time-periodic wakes of circular and square cylinder wakes, and of any body that has reflection symmetry about the wake centre-line. The flow has two synchronous three-dimensional instability modes which exhibit considerable similarity to the long and short wavelength modes observed in bluff-body wakes. In addition, the flow has a new kind of three-dimensional quasi-periodic instability mode that is observable as modulated travelling waves.

The authors would like to thank F. Marques for helpful discussions during preparation of this manuscript, A. Hirsa concerning interpretation of experimental results, D. Barkley and R. D. Henderson for guidance on analysis techniques. This work was supported by the Australian Partnership for Advanced Computing's Merit Allocation Scheme, the Australian Academy of Science's International Scientific Collaborations Program, and NSF Grant CTS-9908599.

REFERENCES

Albensoeder, S., Kuhlmann, H. C. & Rath, H. J. 2001 Three-dimensional centrifugal-flow instabilities in the lid-driven cavity problem. *Phys. Fluids* **13**, 121–135.

Antonijoan, J., Marques, F. & Sanchez, J. 1998 Nonlinear spirals in the Taylor–Couette problem. *Phys. Fluids* **10**, 829–838.

Barkley, D. & Henderson, R. D. 1996 Three-dimensional Floquet stability analysis of the wake of a circular cylinder. *J. Fluid Mech.* **322**, 215–241.

Barkley, D., Tuckerman, L. S. & Golubitsky, M. 2000 Bifurcation theory for three-dimensional flow in the wake of a circular cylinder. *Phys. Rev.* E **61**, 5247–5252.

Bayly, B. J. 1986 Three-dimensional instability of elliptical flow. *Phys. Rev. Lett.* **57**, 2160–2163.

Bayly, B. J. 1988 Three-dimensional centrifugal-type instabilities in inviscid two-dimensional flows. *Phys. Fluids* **31**, 56–64.

Blackburn, H. M. 2002 Three-dimensional instability and state selection in an oscillatory axisymmetric swirling flow. *Phys. Fluids* **14**, 3983–3996.

Blackburn, H. M. & Lopez, J. M. 2003 On three-dimensional quasi-periodic Floquet instabilities of two-dimensional bluff body wakes. *Phys. Fluids* **15**, L57–60.

Chossat, P. & Iooss, G. 1994 *The Couette–Taylor Problem*. Springer.

Crow, S. C. 1970 Stability theory for a pair of trailing vortices. *AIAA J.* **8**, 2172–2179.

Drazin, P. G. & Reid, W. H. 1981 *Hydrodynamic Stability*. Cambridge University Press.

Golubitsky, M., Stewart, I. & Schaeffer, D. G. 1988 *Singularities and Groups in Bifurcation Theory, II*. Springer.

Henderson, R. D. 1997 Nonlinear dynamics and pattern formation in three-dimensional wakes. *J. Fluid Mech.* **352**, 65–112.

Henderson, R. D. 1999 Adaptive spectral element methods for turbulence and transition. In *High-Order Methods for Computational Physics* (ed. T. J. Barth & H. Deconinck), chap. 3, pp. 225–324. Springer.

Henderson, R. D. & Barkley, D. 1996 Secondary instability in the wake of a circular cylinder. *Phys. Fluids* **8**, 1683–1685.

Iooss, G. & Joseph, D. D. 1990 *Elementary Stability and Bifurcation Theory*. Springer.

Karniadakis, G. E. 1990 Spectral element–Fourier methods for incompressible turbulent flows. *Comput. Meth. Appl. Mech. Engng* **80**, 367–380.

Karniadakis, G. E., Israeli, M. & Orszag, S. A. 1991 High-order splitting methods for the incompressible Navier–Stokes equations. *J. Comput. Phys.* **97**, 414–443.

Karniadakis, G. E. & Sherwin, S. J. 1999 *Spectral/hp Element Methods for CFD*. Oxford University Press.

Kuhlmann, H. C., Wanschura, M. & Rath, H. J. 1998 Elliptic instability in two-sided lid-driven cavity flow. *Eur. J. Mech.* B/*Fluids* **17**, 561–569.

Landman, M. J. & Saffman, P. G. 1987 The three-dimensional instability of strained vortices in a viscous fluid. *Phys. Fluids* **30**, 2339–2342.

Laporte, F. & Leweke, T. 2002 Elliptic instability of counter-rotating vortices: experiment and direct numerical simulation. *AIAA J.* **40**, 2483–2494.

Leweke, T. & Williamson, C. H. K. 1998 Cooperative elliptic instability of a vortex pair. *J. Fluid Mech.* **360**, 85–119.

Lopez, J. M. & Hirsa, A. 2001 Oscillatory driven cavity with an air/water interface and an insoluble monolayer: surface viscosity effects. *J. Colloid Interface Sci.* **242**, 1–5.

Lopez, J. M. & Marques, F. 2000 Determining the self-rotation number following a Naimark–Sacker bifurcation in the periodically forced Taylor–Couette flow. *Z. angew. Math. Phys.* **51**, 61–74.

Marques, F., Lopez, J. M. & Blackburn, H. M. 2003 Bifurcations in systems with Z_2 spatio-temporal and $O(2)$ spatial symmetry. *Physica D* (accepted).

Migeon, C. 2002 Details on start-up development of the Taylor–Gortler-like vortices inside a square-section lid-driven cavity for $1000 \leqslant Re \leqslant 3200$. *Exps. Fluids* **33**, 594–602.

Pierrehumbert, R. T. 1986 Universal short-wave instability of two-dimensional eddies in a strained fluid. *Phys. Rev. Lett.* **57**, 2157–2159.

Ramanan, N. & Homsy, G. M. 1994 Linear stability of lid-driven cavity flow. *Phys. Fluids* **6**, 2690–2701.

Robichaux, J., Balachandar, S. & Vanka, S. P. 1999 Three-dimensional Floquet instability of the wake of square cylinder. *Phys. Fluids* **11**, 560–578.

Swift, J. W. & Wiesenfeld, K. 1984 Suppression of period doubling in symmetric systems. *Phys. Rev. Lett.* **52**, 705–708.

Thompson, M. C., Leweke, T. & Williamson, C. H. K. 2001 The physical mechanism of transition in bluff body wakes. *J. Fluids Struct.* **15**, 607–616.

Tuckerman, L. S. & Barkley, D. 2000 Bifurcation analysis for timesteppers. In *Numerical Methods for Bifurcation Problems and Large-Scale Dynamical Systems* (ed. E. Doedel & L. S. Tuckerman), *IMA Volumes in Mathematics and its Applications*, vol. 119, pp. 453–466. Springer.

Vogel, M. J., Hirsa, A. H. & Lopez, J. M. 2003 Spatio-temporal dynamics of a periodically driven cavity flow. *J. Fluid Mech.* **478**, 197–226.

Waleffe, F. 1990 On the three-dimensional instability of strained vortices. *Phys. Fluids* A **2**, 76–80.

Williamson, C. H. K. 1988 The existence of two stages in the transition to three-dimensionality of a cylinder wake. *Phys. Fluids* **31**, 3165–3168.

Williamson, C. H. K. 1996 Three-dimensional wake transition. *J. Fluid Mech.* **328**, 345–407.